

1 INTRODUCTION

2 Above Earth's atmosphere are the Van Allen radiation belts, a toroidally-shaped
3 pair of belts that consist of a complex and dynamic plasma environment. The inner
4 radiation belt is stable, consists of mostly energetic protons, and is located within 2
5 Earth radii (measured near the equator) above Earth's surface. The outer radiation
6 belt, on the other hand, consists of mostly energetic electrons, is highly dynamic
7 on day and hour time scales, and is typically found between 4 and 8 Earth radii
8 above Earth's surface. The radiation belts pose a threat to space exploration due
9 to their effects on our bodies and electrical components. A few effects include: a
10 high radiation dose for manned missions, degradation of silicon causing transistor
11 malfunction, computer memory corruption due to bit flips, etc. With these effects in
12 mind, it is no surprise that the radiation belts have been extensively studied since
13 their discovery in the 1960s.

14 The radiation belt particles, consisting mostly of electrons and protons, are at
15 times unstable to wave growth and generate electric and magnetic waves. These
16 waves can then accelerate and scatter radiation belt particles with a variety of wave-
17 particle mechanisms. These wave-particle interactions are believed to be responsible
18 for scattering electron microbursts, a short and intense increase of precipitating
19 electrons into Earth's atmosphere that are capable of reducing Earth's ozone, and
20 deplete the outer belt's electrons.

21 Electron microbursts, henceforth referred to as microbursts, are typically
22 observed by low Earth orbiting spacecraft, sounding rockets, and high altitude
23 balloons as a sub-second impulse of electrons. Some of the most intense microbursts
24 have electron fluxes that are a factor of 10 to 100 above the background (for example
25 see Fig. 7 in Blake et al. (1996)). Since they were first reported by Anderson and

26 Milton (1964), the intense transient nature of microbursts have compelled countless
27 researchers to pursue an understanding of their properties, their effects on the
28 environment, and the physical mechanism(s) that create microbursts. Microbursts
29 are widely believed to be created by wave-particle scattering between a plasma wave
30 called whistler mode chorus and outer radiation belt electrons, although many details
31 regarding the scattering mechanism are unconstrained or unknown. The goal of this
32 dissertation is to study the wave-particle scattering mechanism that scatters electron
33 microbursts.

34 This chapter serves as an introduction to the fundamental physical concepts
35 that are essential to understand wave-particle interactions in Earth's magnetosphere.
36 We will review the motion of charger particles in electric and magnetic fields, how
37 these particles coalesce organize in the magnetosphere, how particles are accelerated
38 and lost in the magnetosphere, and review the current state of our understanding of
39 microbursts.

40 The rest of this dissertation expands on our current knowledge of microbursts.
41 In Chapter ?? (chapter numbers will be filled in the full dissertation) we will
42 investigate the scattering mechanism responsible for microbursts observed inside the
43 outer radiation belt, near the magnetic equator. Then in Chapters ?? and ?? we
44 will investigate the microburst scattering mechanism indirectly by estimating the
45 microburst footprint size in low Earth orbit and the magnetic equator (near where
46 microburst electrons are believed to be scattered) and compare it to sizes of waves
47 estimated in prior literature.

48 Charged Particle Motion in Electric and Magnetic Fields

A charged particle trapped in the magnetosphere will experience three types of periodic motion in Earth's nearly dipolar magnetic field. The three motions are

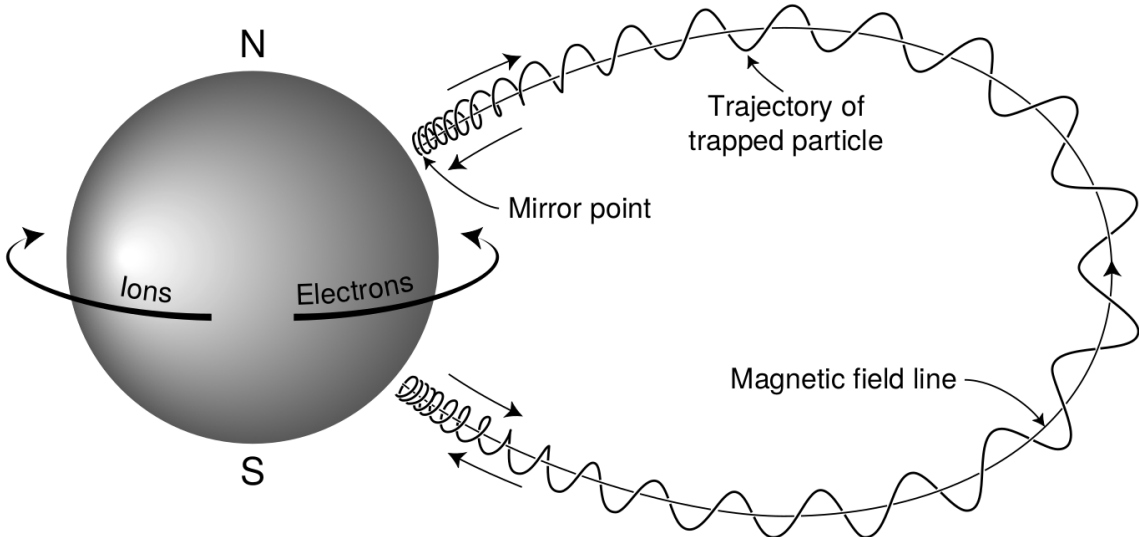


Figure 1.1: The three periodic motions of charged particles in Earth's dipole magnetic field. These motions are: gyration about the magnetic field line, bounce motion between the magnetic poles, and azimuthal drift around the Earth. Figure from (Baumjohann and Treumann, 1997).

ultimately due to the Lorentz force that a particle of momentum \vec{p} , charge q , and velocity \vec{v} experiences in an electric field \vec{E} and magnetic field \vec{B} and is given by

$$\frac{d\vec{p}}{dt} = q(\vec{E} + \vec{v} \times \vec{B}). \quad (1.1)$$

- ⁴⁹ In the magnetosphere, the three periodic motions, in decreasing frequency, are
- ⁵⁰ gyration, bounce, and drift and are schematically shown in Fig. 1.1. Each periodic
- ⁵¹ motion has a corresponding conserved quantity i.e. an adiabatic invariant.

The highest frequency periodic motion is gyration about a magnetic field of magnitude B . This motion is circular with a Larmor radius of

$$r = \frac{mv_{\perp}}{|q|B} \quad (1.2)$$

where m is the mass and v_{\perp} the particle's velocity perpendicular to \vec{B} . This motion

has a corresponding gyrofrequency

$$\Omega = \frac{|q|B}{m} \quad (1.3)$$

in units of radians/second. In the radiation belts, the electron gyrofrequency, Ω_e is on the order of a kHz. The corresponding adiabatic invariant is found by integrating the particle's canonical momentum around the particle's path of gyration

$$J_i = \oint (\vec{p} + q\vec{A}) \cdot d\vec{l} \quad (1.4)$$

where J_i is the i^{th} adiabatic invariant and \vec{A} is the magnetic vector potential. This integral is carried out by integrating the first term over the circumference of the gyro orbit and integrating the second term using Stokes theorem to calculate the magnetic flux enclosed by the gyro orbit. The gyration invariant is $J_1 \sim v_{\perp}^2/B$, which is conserved when the frequency, ω of a force acting on the gyrating electron satisfies

$$\omega \ll \Omega_e.$$

The second highest frequency periodic motion is bouncing due to a parallel gradient in \vec{B} . This periodic motion naturally arises in the magnetosphere because Earth's magnetic field is stronger near the poles, and artificially in the laboratory in magnetic bottle machines. To understand this motion we first we need to define the concept of pitch angle, α as the angle between \vec{B} and \vec{v} which is schematically shown in Fig. 1.2a. The pitch angle relates v with v_{\perp} , and v_{\parallel} (the component of the particles velocity parallel to \vec{B}). As shown in Fig. 1.2b and 1.2c, a smaller (larger) α will increase (decrease) the distance that the charged particle travels parallel to \vec{B} , during one gyration.

Assuming the particle's kinetic energy is conserved, the conservation of J_1 implies that given a particle's $v_{\perp}(0)$ and $B(0)$ at the magnetic equator (where

Earth's magnetic field is usually at a minimum), we can calculate its $v_{\perp}(s)$ along the particle's path s by calculating $B(s)$ from magnetic field models. Thus the particle's perpendicular velocity is then related via

$$\frac{v_{\perp}^2(0)}{B(0)} = \frac{v_{\perp}^2(s)}{B(s)} \quad (1.5)$$

⁶⁷ which can be rewritten as

$$\frac{v^2 \sin^2 \alpha(0)}{B(0)} = \frac{v^2 - v_{\parallel}^2(s)}{B(s)} \quad (1.6)$$

⁶⁸ and re-arranged to solve for $v_{\parallel}(s)$

$$v_{\parallel}(s) = v \sqrt{1 - \frac{B(s)}{B(0)} \sin^2 \alpha(0)} \quad (1.7)$$

⁶⁹ which will tend towards 0 when the second term in the radical approaches 1.

⁷⁰ The location where $v_{\parallel}(s) = 0$ is called the mirror point and is where a particle
⁷¹ reverses direction. Since Earth's magnetic field is stronger towards the poles, the
⁷² mirroring particle will execute periodic bounce motion between its two mirror points
⁷³ in the northern and southern hemispheres. The corresponding adiabatic invariant, J_2
⁷⁴ is

$$J_2 = \oint p_{\parallel} ds \quad (1.8)$$

where ds describes the particle path between the mirror points in the northern and southern hemispheres (see Fig. 1.1). J_2 is found by substituting Eq. 1.7 into Eq. 1.8 and defining the magnetic field strength at the mirror points as B_m (where $\alpha(m) =$

90°). The J_2 integral can be written as

$$J_2 = 2p \int_{m_n}^{m_s} \sqrt{1 - \frac{B(s)}{B(m)}} ds \quad (1.9)$$

where m_n and m_s are the northern and southern mirror points, respectively. The bounce period can be estimated (e.g. Baumjohann and Treumann, 1997) to be

$$t_b \approx \frac{LR_e}{\sqrt{W/m}} (3.7 - 1.6 \sin \alpha(0)) \quad (1.10)$$

where W is the particle's kinetic energy, and L is the L -shell. L -shell describes the distance from the Earth's center to the location where a particular magnetic field line crosses the magnetic equator, in units of Earth radii, R_e . As with gyration, the particle will bounce between the mirror points as long as $\omega \ll \Omega_b$, where Ω_b is the bounce frequency.

At this stage it is instructional to introduce the notion of the loss cone pitch angle, α_L . A particle with $\alpha \leq \alpha_L$ will mirror at or below ≈ 100 km altitude in the atmosphere. A charged particle gyrating at those altitudes will encounter and Coulomb scatter with the dense atmosphere and be lost from the magnetosphere.

The slowest periodic motion experienced by charged particles in Earth's magnetic field is azimuthal drift around the Earth. This drift results from a combination of a radial gradient in \vec{B} and the curvature of the magnetic field. The radial gradient drift arises because Earth's magnetic field is stronger near the Earth where the particle's gyroradius radius of curvature shrinks as it gyrates towards stronger magnetic field, and expands when it gyrates outward. The overall effect is the particle gyro orbit does not close on itself and negatively charged particles drift east and positively charged particles drift west. The radial gradient drift is further enhanced by the centrifugal force that a particle experiences as it bounces along the curved field lines. The drift

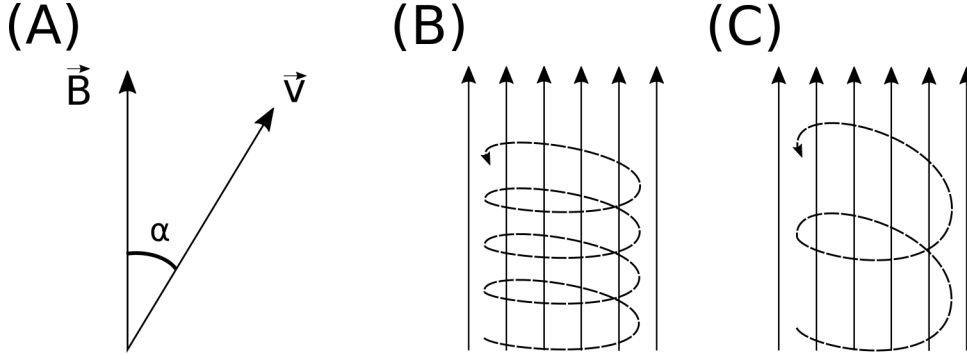


Figure 1.2: Charged particle motion in a uniform magnetic field \vec{B} . Panel (A) shows the geometry defining the pitch angle, α . Panel (B) and (C) show two helical electron trajectories with dashed lines assuming a large and small α (corresponding to a small and large parallel velocity $v_{||}$), respectively.

95 adiabatic invariant, J_3 is found by integrating Eq. 1.4 over the complete particle orbit
 96 around the Earth. The shape of this drift orbit is known as a drift shell. For J_3 , the
 97 first term is negligible and the second term is the magnetic flux enclosed by the drift
 98 shell, Φ_m i.e. $J_3 \sim \Phi_m$.

99 Figure 1.3 from Schulz and Lanzerotti (1974) shows contours of the gyration,
 100 bounce, and drift frequencies for electrons and protons in Earth's dipole magnetic
 101 field.

Up until now we have considered the three periodic motions due Earth's magnetic field in the absence of electric fields. If there is an electric field, E_{\perp} perpendicular to \vec{B} , a particle's center of gyration i.e., averaged position of the particle over a gyration, will drift with a velocity perpendicular to both E_{\perp} and \vec{B} . The drift velocity can be solved using Eq. 1.1 and is

$$\vec{v}_E = \frac{\vec{E} \times \vec{B}}{B^2}. \quad (1.11)$$

102 If there is a parallel magnetic field, $E_{||}$ then the particle is accelerated along the
 103 magnetic field line. An $E_{||}$ pointing away from the Earth will contribute to the mirror
 104 force and raise the particle's mirror point. On the contrary, an Earthward pointing

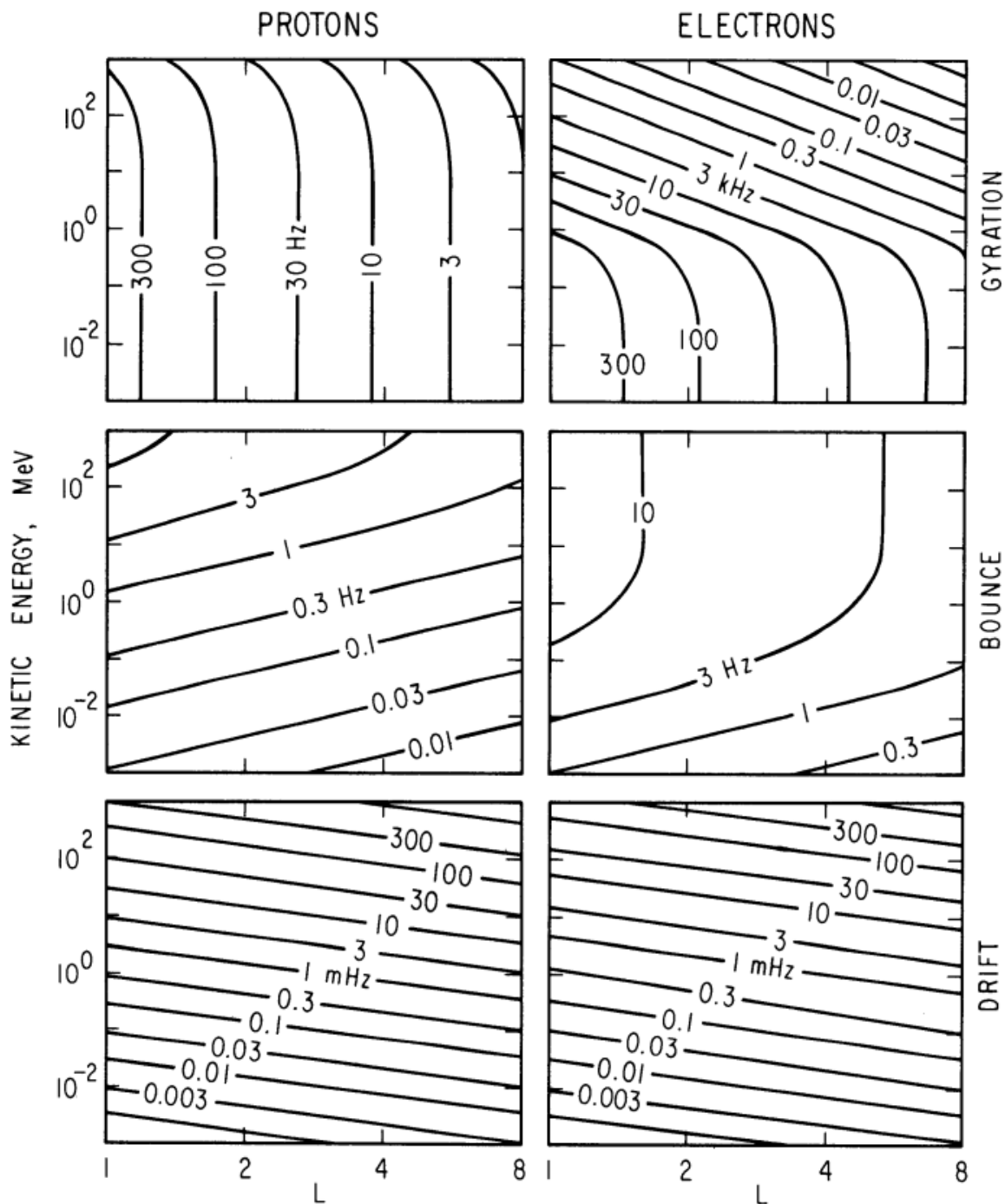


Figure 1.3: Contours of constant gyration, bounce, and drift frequencies for electrons and protons in a dipole field. Figure from Schulz and Lanzerotti (1974).

105 $E_{||}$ will oppose the mirror force and lower the mirror point. If the Earthward $E_{||}$ is
106 strong enough, the mirror point is lowered into the atmosphere that will precipitate
107 particles. This is the mechanism that generates the aurora.

108 Particle Populations and Their Interractions in the Magnetosphere

109 Now that we have looked at the dynamics of single-particle motion in electric
110 and magnetic fields, we will briefly tour the various macroscopic populations in the
111 magnetosphere that are illustrated in Fig. 1.4.

112 The sun and its solar wind are ultimately the source of energy input into the
113 magnetosphere. The solar wind at Earth's orbit is a plasma traveling at supersonic
114 speeds with an embedded interplanetary magnetic field (IMF). When the solar wind
115 encounters Earth's magnetic field, the plasma can not easily penetrate into the
116 magnetosphere because the plasma is frozen-in on magnetic field lines. Thus the
117 plasma and its magnetic field drapes around the magnetosphere, forming a cavity in
118 the solar wind that qualitatively has a shape as shown in Fig. 1.4. Because the solar
119 wind is supersonic at 1 AU, a bow shock exists upstream of the magnetosphere.
120 The solar wind plasma, after it is shocked by the bow shock, flows around the
121 magnetosphere inside the magnetosheath. The surface where the solar wind ram
122 pressure and Earth's magnetic pressure balance is termed the magnetopause, which
123 can be thought of as a boundary between the solar wind and Earth's magnetosphere.
124 This is a slightly naive description of the magnetopause, but is nonetheless an
125 instructive conceptual picture. The shocked plasma then flows past the Earth where
126 it shapes the magnetotail. In the magnetotail the magnetopause exists where the solar
127 wind magnetic pressure balances Earth's magnetic field pressure in the lobes. The
128 magnetotail extends on the order of $100 R_E$ downstream of Earth, and the tailward
129 stretching of magnetic field lines creates the plasma sheet which exists in the region

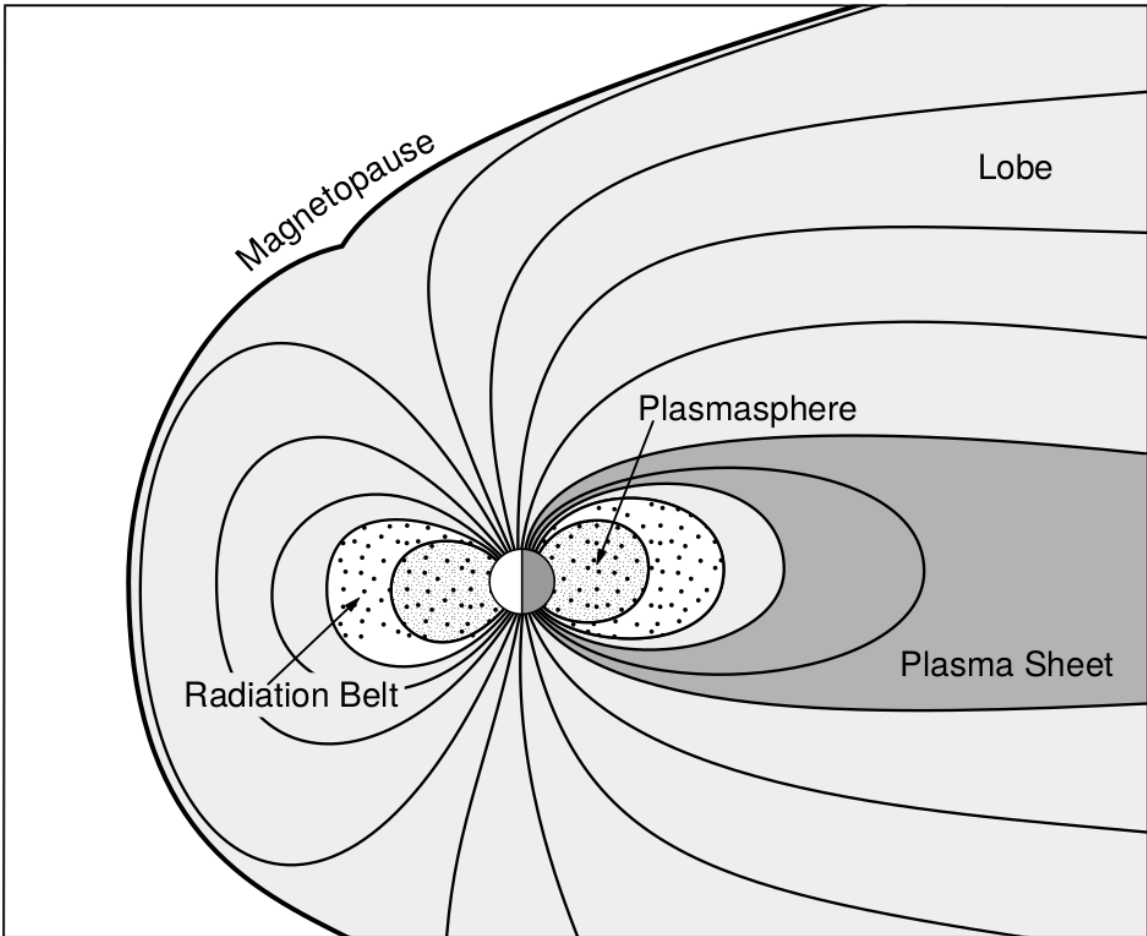


Figure 1.4: A few macroscopic structures in the magnetosphere. The magnetosphere boundary with the solar wind is the magnetopause. The magnetotail consists of two lobes that contain Earth's magnetic flux with the plasma sheet separating the two lobes. The inner magnetosphere contains the plasmasphere, the ring current, and the radiation belts which are co-located. Figure from Baumjohann and Treumann (1997).

₁₃₀ of low magnetic field strength near the magnetic equator (e.g. Eastwood et al., 2015).

₁₃₁ Populations in the Inner Magnetosphere

₁₃₂ Closer to Earth, where the magnetic field is largely dipolar, are three plasma
₁₃₃ populations that comprise the inner magnetosphere: the plasmasphere, the ring
₁₃₄ current, and the radiation belts which are shown in Fig. 1.4. Before we describe these
₁₃₅ three particle populations in detail, we will first introduce the coordinate system that
₁₃₆ most naturally describes the inner magnetosphere environment, and then the electric
₁₃₇ fields that effect mostly low energy particles.

₁₃₈ In this coordinate system the “radial” coordinate was defined in section 1 and
₁₃₉ is the L shell. The azimuthal coordinate is the magnetic local time (MLT). For an
₁₄₀ observer above Earth’s north pole looking down, MLT is defined to be 0 (midnight)
₁₄₁ in the anti-sunward direction, and increases in the counter-clockwise direction with 6
₁₄₂ at dawn, 12 at noon (sunward direction), and 18 in dusk. The final coordinate is the
₁₄₃ magnetic latitude, λ which is analogous to the latitude coordinate in the spherical
₁₄₄ coordinate system, and is defined to be 0 at the magnetic equator. This coordinate
₁₄₅ system is shown in Fig. 1.5 and naturally describes the inner magnetosphere
₁₄₆ populations described below.

₁₄₇ The low energy particle dynamics in the inner magnetosphere are organized by
₁₄₈ two electric fields: the co-rotation and the dawn-dusk electric fields. The co-rotation
₁₄₉ electric field arises from Earth’s rotation. The magnetic field and the particles frozen
₁₅₀ on it rotate with the Earth. To a non-rotating observer this rotation appears as a
₁₅₁ radial electric field that drops off as $\sim L^{-2}$. The other electric field, pointing from
₁₅₂ dawn to dusk is called the convection electric field and is due to the Earthward
₁₅₃ transport of particles from the magnetotail that appears as an electric field in Earth’s
₁₅₄ reference frame. The superposition of the co-rotation and convection electric

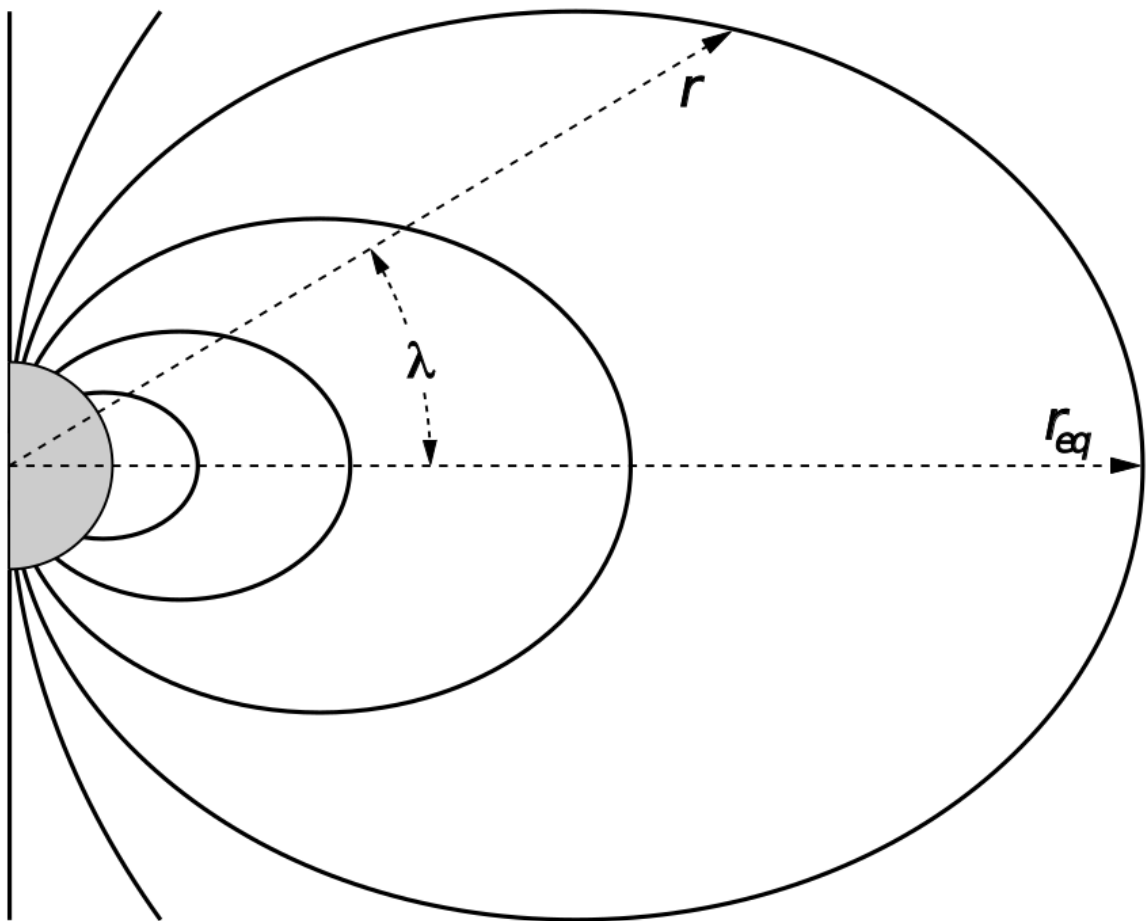


Figure 1.5: The dipole coordinate system. The magnetic latitude of \mathbf{r} is λ . The radial distance to a magnetic field line in the equatorial plane is typically given by $L = r_{eq}/R_e$. Figure from Baumjohann and Treumann (1997).

fields is a potential field shown in Fig. 1.6. The shaded area in Fig. 1.6 shows the orbits on which low energy electrons are trapped, and outside this region the particles are not trapped. The dynamic topology of the shaded region in Fig. 1.6 is controlled by only the convection electric field which is dependent on the solar wind speed and the IMF. The lowest energy particles that orbit in the shaded region in Fig. 1.6 make up the plasmasphere.

Plasmasphere The plasmasphere is a dense ($n_e \sim 10^3/\text{cm}^3$), cool ($\sim \text{eV}$) plasma. The plasmasphere typically extends to $L \sim 4$ and the spatial extent is highly dependent on the solar wind and magnetospheric conditions. The source of the plasmasphere is the ionosphere. The two main mechanisms that fill the plasmasphere with cold plasma are ionization of the ionosphere by sunlight and particle precipitation. The ultraviolet ionization by sunlight is strongly dependent on the time of day (day vs night), latitude (more ionization near the equator). The ionization due to particle precipitation, on the other hand, is highly dependent on magnetospheric conditions, and mostly occurs at high latitudes.

The outer boundary of the plasmasphere is the plasmapause which is typically identified as a steep radial gradient in plasma density from $\sim 10^3/\text{cm}^3$ to $\sim 1/\text{cm}^3$. The location of the plasmapause is important to model (e.g. O'Brien and Moldwin, 2003) and understand since the plasma density strongly controls the efficiency of particle scattering by waves (e.g. Horne et al., 2005).

Ring Current The next higher energy population is the ring current. This population consists of protons and electrons between tens and a few hundred keV that drift around the Earth. The orbits of higher energy particles are not as effected by the convection and co-rotation electric field, rather they drift around the Earth due to gradient and curvature drifts. Since the direction of the drift is dependent on

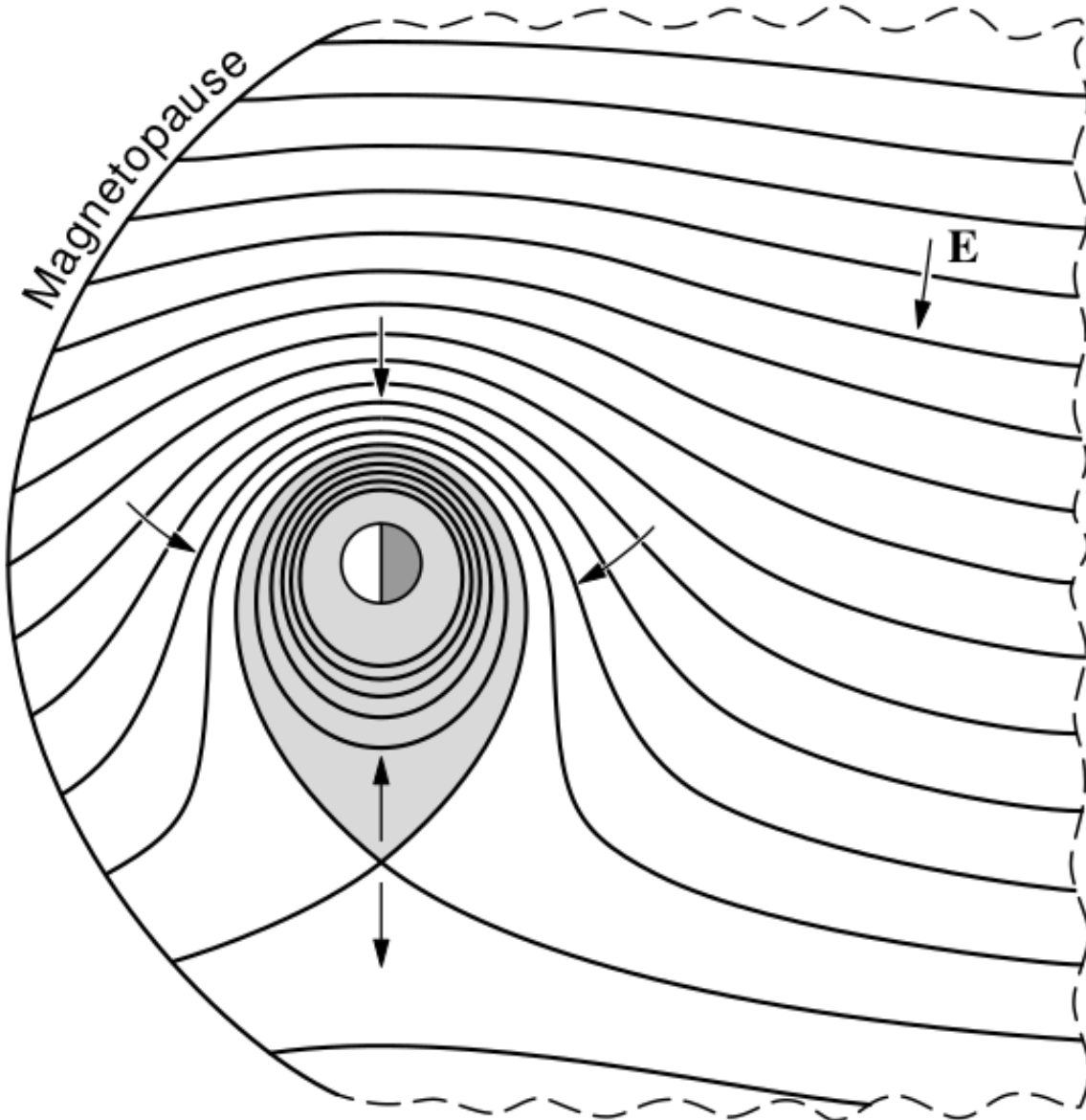


Figure 1.6: Equipotential lines and electric field arrows due to the superposition of the co-rotation and convection electric fields. Electrons in the shaded region execute closed orbits. Outside of the shaded regions the electrons are not trapped and will escape. The region separating the two regimes is called the Alfvén layer. Figure from Baumjohann and Treumann (1997).

180 charge, protons drift west around the Earth and electrons drift East. This has the
181 effect of creating a current around the Earth.

182 The ring current generates a magnetic field which decreases the magnetic field
183 strength at the surface of the Earth and increases it outside of the ring current.
184 The decrease of Earth's magnetic field strength is readily observed by a system of
185 ground-based magnetometers and is merged into a Disturbance Storm Time (DST)
186 index to quantify the global reduction in the magnetic field. An example of a DST
187 index time series from the 2015 St. Patrick's Day storm, driven by a coronal mass
188 ejection (CME), is shown in Fig. 1.7. A few notable features of the storm and the
189 ring current are worth pointing out. At the start of the storm the ring current is
190 sometimes depleted and DST increases slightly (termed the initial phase or sudden
191 storm commencement). Then the ring current population is rapidly built up and
192 DST rapidly decreases during the main phase. Lastly, after the storm passes, the
193 ring current gradually decays toward its equilibrium state over a period of a few
194 days and DST returns towards 0 during the recovery phase. The DST index (along
195 with other geomagnetic indices) are readily used by the space physics community to
196 quantify the global state of the magnetosphere.

197 Radiation Belts The highest particle energy populations are in the Van Allen
198 radiation belts. These belts were discovered by Van Allen (1959) and Vernov and
199 Chudakov (1960) during the Cold War and are a pair of toroidally shaped populations
200 of trapped electrons and protons shown in Fig. 1.8. Their quiescent toroidal shape,
201 similar to the shape of the plasmasphere and ring current, is a result of Earth's dipole
202 magnetic field.

203 The inner radiation belt is extremely stable on time periods of years, extends
204 to $L \approx 2$, and mainly consists of protons with energies between MeV and GeV and

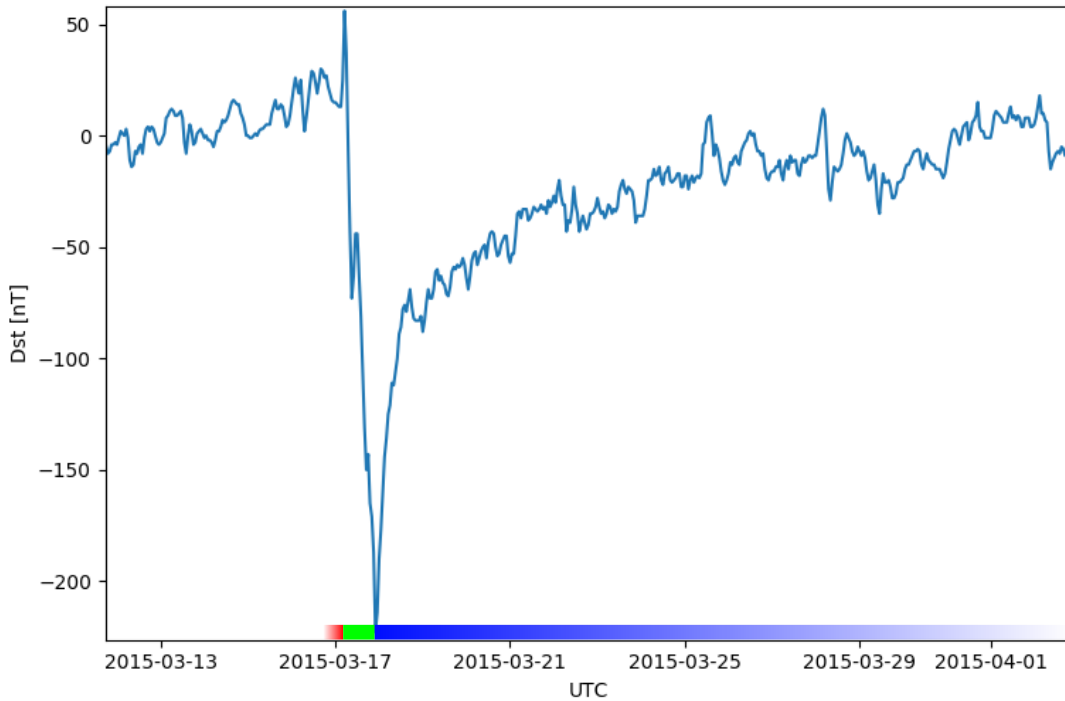


Figure 1.7: The DST index during the St. Patrick's Day 2015 storm. This storm was caused by a coronal mass ejection on March 15th, 2015. The storm phases are: initial phase, main phase, and recovery phase. The initial phase occurred when the Dst peaked at $+50$ nT on March 17th during which the ring current was eroded by the coronal mass ejection during the interval shown by the red bar shown at the bottom. Then the following rapid decrease to ≈ -200 nT was during the main phase where many injections from the magnetotail enhanced the ring current, which reduced Earth's magnetic field strength at the ground, and is shown with the green bar. Lastly, the recovery phase lasted from March 18th to approximately March 29th during which the ring current particles were lost and the ring current returned to its equilibrium state. The recovery phase is shown with the blue bar.

The Earth's Electron Radiation Belts

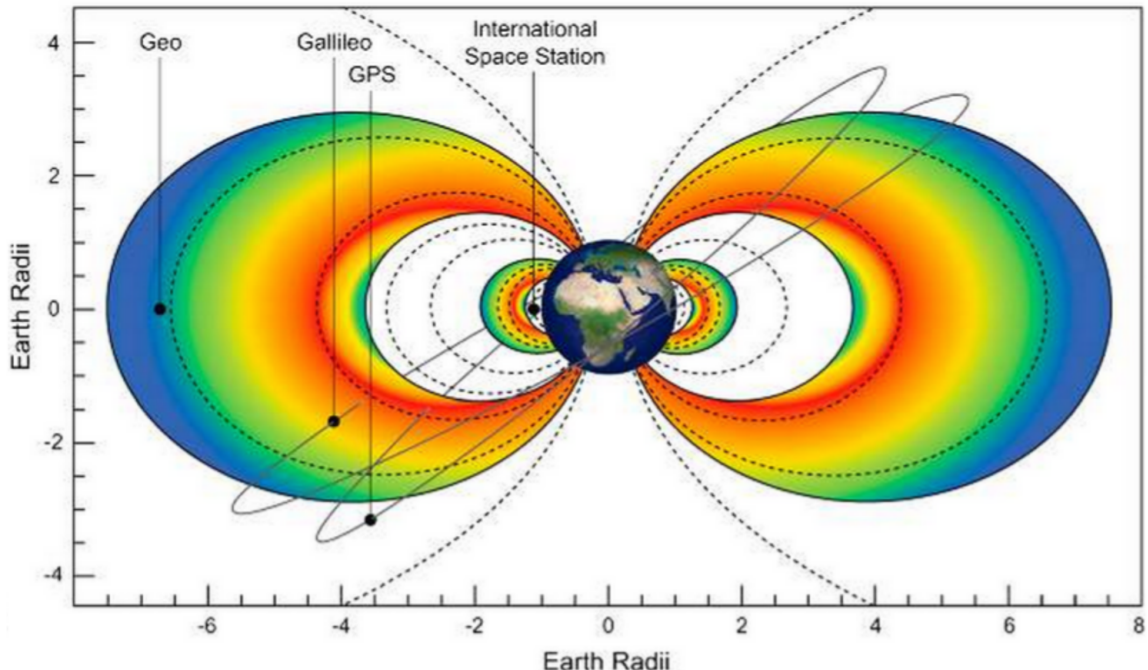


Figure 1.8: The two radiation belts with the locations of various satellites and orbits. Figure from (Horne et al., 2013).

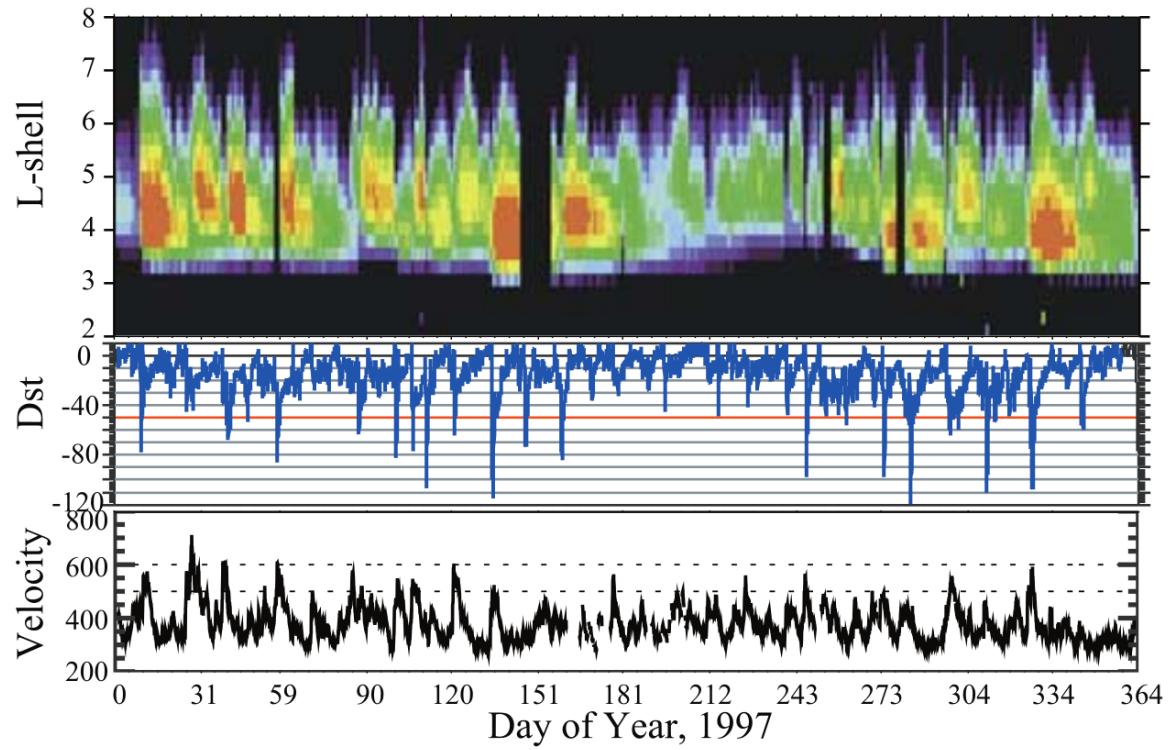


Figure 1.9: The dynamics of the outer radiation belt in 1997 from the POLAR satellite. Top panel shows the 1.2-2.4 MeV electron flux as a function of L and 1997 day of year. The middle panel shows the DST index, and bottom panel shows the solar wind velocity. Figure from (Reeves et al., 2003).

205 electrons with energies up to ≈ 1 MeV (Claudepierre et al., 2019). The source of
 206 inner radiation belt protons is believed to be due to cosmic-ray albedo neutron decay
 207 (e.g. Li et al., 2017) and inward radial diffusion for electrons (e.g. O'Brien et al.,
 208 2016). The gap between the inner and outer radiation belt is called the slot, which is
 209 believed to be due to hiss waves inside the plasmasphere (described below) scattering
 210 particles into the atmosphere (e.g. Breneman et al., 2015; Lyons and Thorne, 1973).

211 The outer radiation belt is much more dynamic and consists of mainly electrons
 212 of energies up to a few MeV. The outer belt's spatial extent is highly variable as
 213 shown in Fig. 1.9, and is typically observed between L of 4 and 8. The source of
 214 outer radiation belt electrons is widely believed to be injections of plasma from the
 215 magnetotail that is then accelerated to high energies.

216 Due to the highly energetic and dynamic nature of the radiation belts, and their
 217 impact on human presence in space, the radiation belts have been studied for over
 218 half century. Researchers have studied and attempted to predict the dynamics of
 219 radiation belt particles, waves, and wave-particle interactions by considering various
 220 competing particle acceleration and loss mechanisms which are described next.

221 Radiation Belt Particle Sources and Sinks

222 Adiabatic Heating

223 One of the particle heating and transport mechanisms arises from the Earthward
 224 convection of particles. The conservation of J_1 implies that the initial and final v_\perp
 225 depends on the change in the magnetic field amplitude

$$\frac{v_{\perp i}^2}{B_i} = \frac{v_{\perp f}^2}{B_f}. \quad (1.12)$$

²²⁶ As a particle convects Earthward, $B_f > B_i$ thus v_{\perp} must increase. The dipole
²²⁷ magnetic field amplitude can be written as

$$B(L, \theta) = \frac{31.2 \text{ } \mu\text{T}}{L^3} \sqrt{1 + 3 \cos^2 \theta}. \quad (1.13)$$

²²⁸ The change in v_{\perp}^2 can be found by taking the ratio of $B(L, \theta)$ at two different L shells

$$\frac{v_{\perp f}^2}{v_{\perp i}^2} = \left(\frac{L_i}{L_f} \right)^3 \quad (1.14)$$

²²⁹ thus the increase in $v_{\perp} \sim (L_i/L_f)^{3/2}$.

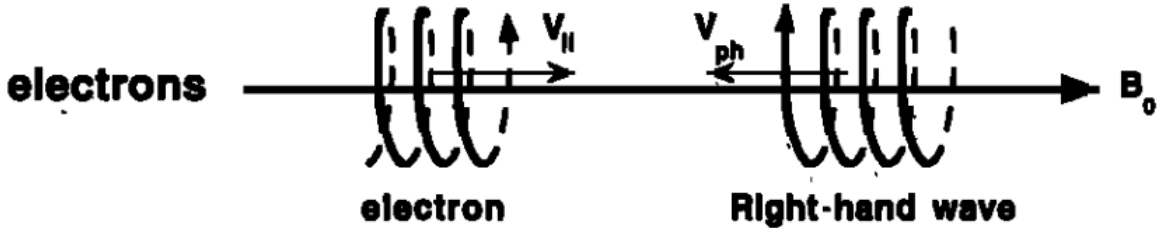
²³⁰ As the particle convects Earthward its v_{\parallel} also increases because the distance
²³¹ between the particle's mirror points decrease. If J_2 is conserved, the shrinking bounce
²³² path implies that v_{\parallel} must increase by

$$\frac{v_{\parallel f}^2}{v_{\parallel i}^2} = \left(\frac{L_i}{L_f} \right)^k \quad (1.15)$$

²³³ where k ranges from 2 for equatorial pitch angles, $\alpha_{eq} = 0^\circ$, to 2.5 for $\alpha_{eq} = 90^\circ$
²³⁴ (Baumjohann and Treumann, 1997). Since the rate of adiabatic heating is greater in
²³⁵ the perpendicular direction than heating in the parallel direction, an initially isotropic
²³⁶ particle distribution will become anisotropic during its convection. These isotropic
²³⁷ particles can then become unstable to wave growth and generate waves in order to
²³⁸ reach equilibrium.

²³⁹ Wave Resonance Heating

²⁴⁰ Another mechanism that heats particles is due to particles resonating with
²⁴¹ plasma waves. A few of the electromagnetic wave modes responsible for particle
²⁴² acceleration (and scattering) relevant to radiation belt dynamics are hiss, whistler
²⁴³ mode chorus (chorus), and electromagnetic ion cyclotron (EMIC) waves. These waves



$$\omega + k_{\parallel} v_{\parallel} = \Omega^-$$

Figure 1.10: The trajectories of an electron and a right-hand circularly polarized wave during a cyclotron resonance. The electron's v_{\parallel} and the wave's k_{\parallel} are in opposite directions such that the wave's frequency is Doppler shifted to an integer multiple of the electron cyclotron frequency. Figure from (Tsurutani and Lakhina, 1997).

244 are created by the loss cone instability that is driven by an anisotropy of electrons for
 245 chorus waves, and protons for EMIC waves. The level of anisotropy can be quantified
 246 by the ratio of the perpendicular to parallel particle temperatures (T_{\perp}/T_{\parallel}). A particle
 247 distribution is unstable when $T_{\perp}/T_{\parallel} > 1$. Since electrons gyrate in a right-handed
 248 sense, the chorus waves also tend to be right hand circularly polarized (Tsurutani and
 249 Lakhina, 1997). The same argument also applies to protons and left hand circularly
 250 polarized EMIC waves.

251 These circularly polarized waves can resonate with electrons and/or protons
 252 when their relative motion results in a static \vec{E} . One example of a resonance between
 253 a right hand circularly polarized wave and an electron is shown in Fig. 1.10. The
 254 electron's v_{\parallel} and the wave's parallel wave vector, k_{\parallel} are in opposite directions such
 255 that the wave frequency ω is Doppler shifted to an integer multiple of the Ω_e where the
 256 electron feels a static electric field and is accelerated or decelerated. Quantitatively,
 257 this resonance condition is easier to understand with the following toy model.

258 Assume a uniform magnetic field $\vec{B} = B_0 \hat{z}$ with a parallel propagating ($k = k \hat{z}$),
 259 right-hand circularly polarized wave. The wave's electric field as a function of position

²⁶⁰ and time can be written as

$$\vec{E} = E_0(\cos(\omega t - kz)\hat{x} + \sin(\omega t - kz)\hat{y}). \quad (1.16)$$

The angular component of \vec{E} that will effect the particle's v_{\perp} is

$$E_{\theta} = \vec{E} \cdot \hat{\theta} = E_0 \cos(\omega t - kz + \theta). \quad (1.17)$$

²⁶¹ Now assume that the electron is traveling in the $-\hat{z}$ direction with a velocity $\vec{v} = -v_0\hat{z}$
²⁶² so its time dependent position along \hat{z} is

$$z(t) = -v_0t \quad (1.18)$$

²⁶³ and gyrophase is

$$\theta(t) = -\Omega t + \theta(0) \quad (1.19)$$

²⁶⁴ where the first negative sign comes from the electron's negative charge. Now we put
²⁶⁵ this all together and find the force that the electron will experience

$$m \frac{dv_{\theta}}{dt} = qE_{\theta} = qE_0 \sin((\omega + kv_0 - \Omega)t + \theta(0)). \quad (1.20)$$

²⁶⁶ This is a relatively complex expression, but when the time dependent component is
²⁶⁷ 0, i.e.

$$\omega + kv_0 - \Omega = 0, \quad (1.21)$$

²⁶⁸ the electron will feel a static electric field and be accelerated or decelerated depending
²⁶⁹ on θ_0 , the phase between the wave and the electron. The expression in Eq. 1.21 is

270 commonly referred to as the resonance condition and is more generally written as

$$\omega - k_{||}v_{||} = \frac{n\Omega_e}{\gamma} \quad (1.22)$$

271 where n is the resonance order, and γ is the relativistic correction (e.g. Millan and
 272 Thorne, 2007). In the case of the cyclotron resonance, $\omega \approx \Omega_e$ thus J_1 is violated.
 273 Since J_1 is violated, J_2 and J_3 are also violated since the conditions required to violate
 274 J_2 and J_3 are less stringent than J_1 . It is important to remember that a particle will
 275 experience the effects of many waves along its drift orbit. The typical MLT extent
 276 of a handful of waves that are capable of resonating with radiation belt electrons are
 277 shown in Fig. 1.11.

278 Particle Losses

279 Now that we have seen two general mechanisms with which particles are
 280 accelerated in the magnetosphere, we will now consider a few specific mechanisms
 281 that remove particles from the magnetosphere into the atmosphere or the solar
 282 wind. One mechanism that transports magnetosperic particles into the solar wind
 283 is magnetopause shadowing (e.g. Ukhorskiy et al., 2006). Magnetopause shadowing
 284 occurs when the ring current is strengthened and Earth's magnetic field strength is
 285 increased outside of the ring current. If the ring current increases slowly enough (such
 286 that J_3 is conserved), a particle drift shell will move outward to conserve J_3 . If the
 287 particle's drift shell expands past the magnetopause, the particle will be lost to the
 288 solar wind.

289 **Make sure I understand ULF waves and radial diffusion right** Another particle
 290 loss (and acceleration) mechanism is driven by ultra low frequency (ULF) waves and
 291 is called radial diffusion. Radial diffusion is the transport of particles from high
 292 to low phase space density, f . If the transport is radially inward, particles will

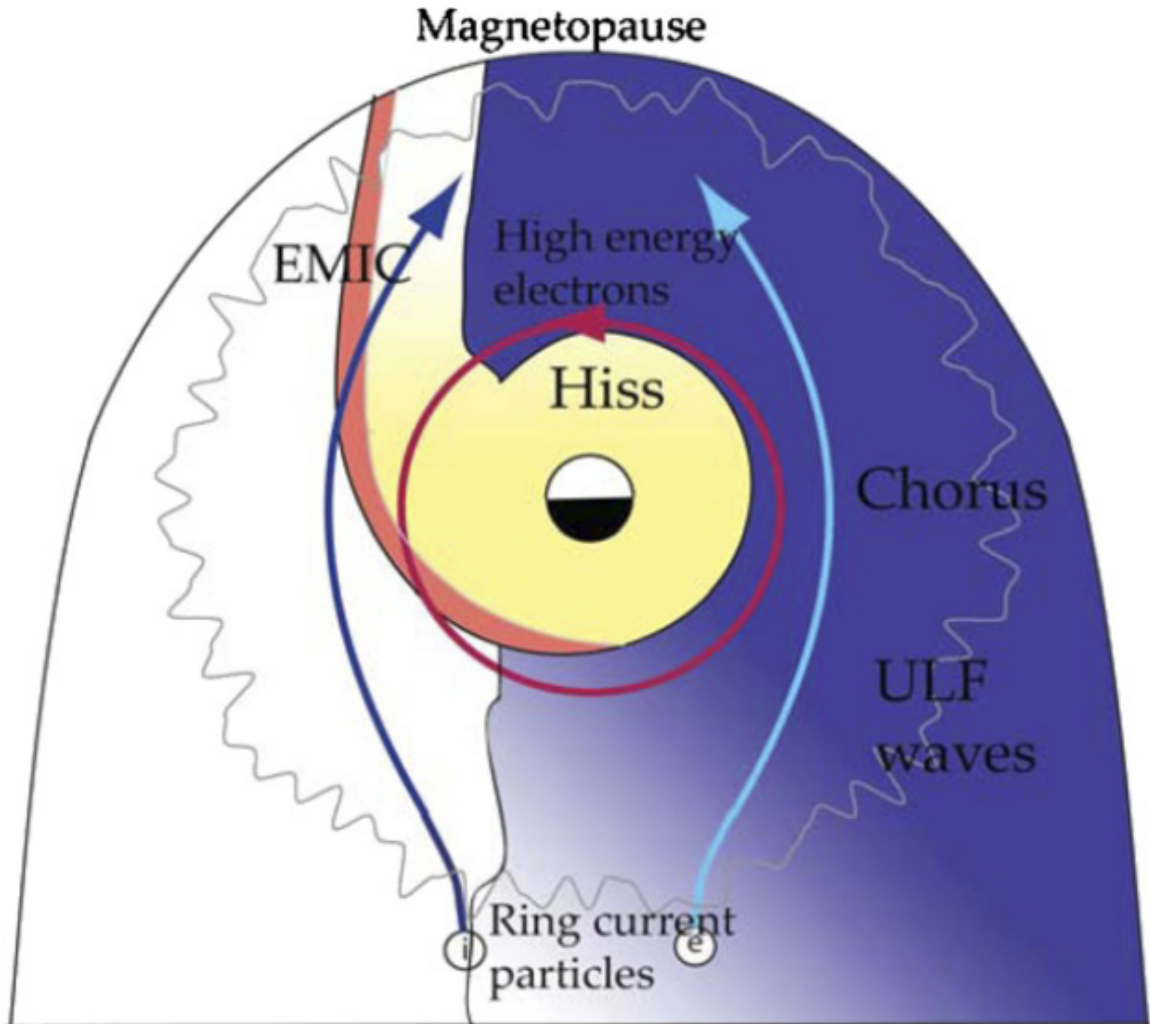


Figure 1.11: Various wave modes in the magnetosphere. Ultra low frequency waves occur through the magnetosphere. Chorus waves are typically observed in the 0-12 midnight-dawn region. EMIC waves are typically observed in the dusk MLT sector. Hiss waves are observed inside the plasmasphere. Figure from Millan and Thorne (2007).

293 appear to be accelerated. On the other hand, radially outward radial diffusion can
 294 transport particles through the magnetopause where they will be lost to the solar
 295 wind. Reeves et al. (2013) investigated the driver of particle acceleration during the
 296 October 2012 storm and observationally found that inward radial diffusion was not
 297 dominant, rather local acceleration via wave-resonance heating appeared to be the
 298 dominant acceleration mechanism.

299 The loss mechanism central to this dissertation is pitch angle and energy
 300 scattering of electrons by waves. Some of the waves that scatter electrons in energy
 301 and pitch angle in the inner magnetosphere are: plasmaspheric hiss (e.g. Breneman
 302 et al., 2015; O'Brien et al., 2014), EMIC waves (e.g. Capannolo et al., 2019; Hendry
 303 et al., 2017), and chorus waves (e.g. Breneman et al., 2017; Kasahara et al., 2018;
 304 Ozaki et al., 2019). These wave-particle interactions occur when the resonance
 305 condition in Eq. 1.22 is satisfied and the particle's energy and α is modified by
 306 the wave. More details regarding the theory of pitch angle and energy diffusion is
 307 given in Chapter ???. If the wave changes α towards 0 and $\alpha < \alpha_L$, then the particle's
 308 mirror point dips below 100 km altitude where the particle can be lost from the
 309 magnetosphere. One manifestation of pitch angle scattering of particles into the loss
 310 cone are microbursts: a sub-second durtaison impulse of electrons.

311

Microbursts

312 Microbursts were first with high altitude balloons which measured bremsstrahlung
 313 X-rays emitted by microburst electrons impacting the atmosphere by Anderson
 314 and Milton (1964). In the following years, numerous balloon flights expanded our
 315 knowledge of non-relativistic ($\lesssim 500$ keV) microbursts (relativistic microbursts have
 316 not yet been observed by high altitude balloons) by quantifying the microburst spatial
 317 extent, temporal width, occurrence frequency, extent in L and MLT, and their source.

318 The microburst source was first believed to be either a local plasma instability or a
 319 propagating disturbance in the magnetosphere (Barcus et al., 1966; Brown et al., 1965;
 320 Parks, 1967; Trefall et al., 1966). Soon after, both non-relativistic and relativistic
 321 microbursts electrons were directly observed in LEO with spacecraft including the
 322 Solar Anomalous and Magnetospheric Particle Explorer (SAMPEX) (e.g. Blake et al.,
 323 1996; Blum et al., 2015; Douma et al., 2019, 2017; Greeley et al., 2019; Lorentzen et al.,
 324 2001a,b; Nakamura et al., 1995, 2000; O'Brien et al., 2004, 2003), Montana State
 325 University's (MSU) Focused Investigation of Relativistic Electron Bursts: Intensity,
 326 Range, and Dynamics II (FIREBIRD-II) (Anderson et al., 2017; Breneman et al.,
 327 2017; Crew et al., 2016; Klumpar et al., 2015; Spence et al., 2012), and Science
 328 Technologies Satellite (STSAT-I) (e.g. Lee et al., 2012, 2005). An example microburst
 329 time series is shown in Fig. 1.12 and was observed by the FIREBIRD-II CubeSats.
 330 The prominent features of the example microbursts in Fig. 1.12 are their sub-second
 331 duration, half order of magnitude increase in count rate above the falling background,
 332 and their 200-800 keV energy extent.

333 Microbursts are observed on magnetic field footprints that are connected to the
 334 outer radiation belt (approximately $4 < L < 8$). They are predominately observed in
 335 the 0-12 MLT sector with an elevated occurrence frequency during magnetospherically
 336 disturbed times as shown in Fig. 1.13 (e.g. Douma et al., 2017). O'Brien et al. (2003)
 337 used SAMPEX relativistic electron data and found that microbursts predominately
 338 occur during the main phase of storms, with a heightened occurrence rate during the
 339 recovery phase. Microburst occurrence rates are also higher during high solar wind
 340 velocity events e.g. from co-rotating interaction regions (Greeley et al., 2019; O'Brien
 341 et al., 2003).

342 The estimated impact of microbursts on the atmosphere and the radiation
 343 belts is significant. Relativistic microburst electrons impacting the atmosphere are

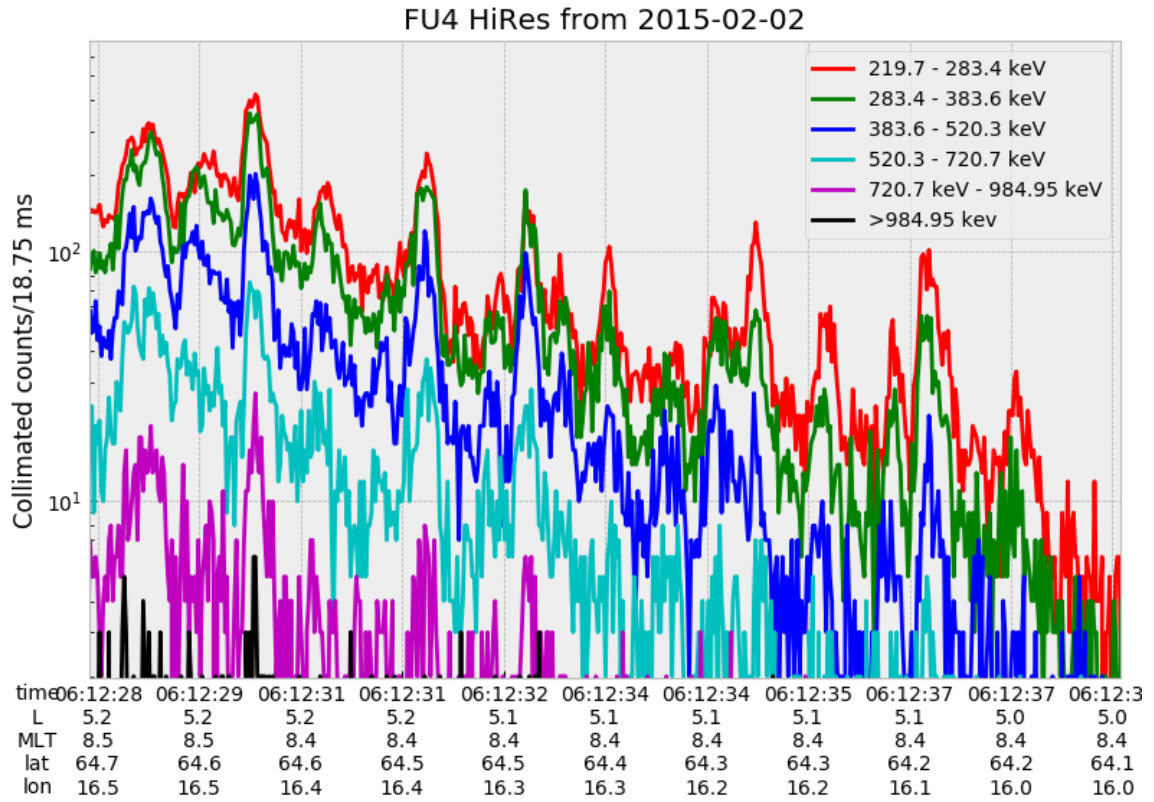


Figure 1.12: An example train of microbursts observed by FIREBIRD-II unit 4 on February 2nd, 2015. The colored curves show the differential energy channel count rates in five channels from ≈ 200 keV to 1 MeV and a sixth integral energy channel with a 1 MeV threshold. The x-axis labels show auxiliary information such as time of observation and the spacecraft position in L, MLT, latitude and longitude coordinates.

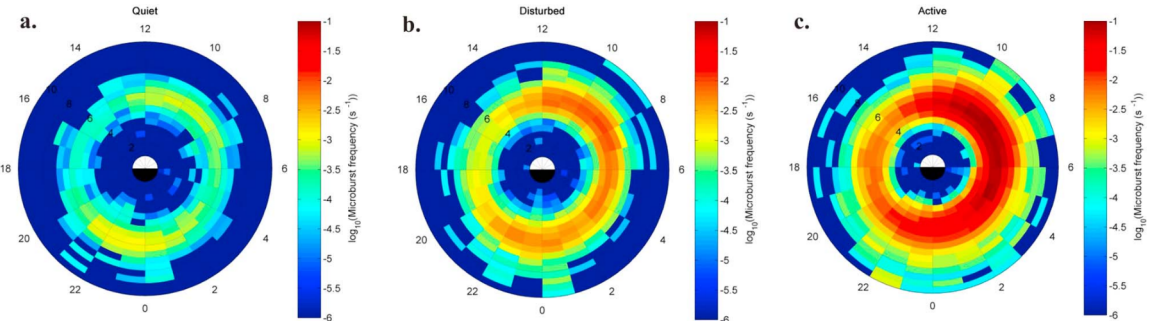


Figure 1.13: Distribution of > 1 MeV microburst occurrence rates as a function of L and MLT. The three panels show the microburst occurrence rate dependence on geomagnetic activity, parameterized by the auroral electrojet (AE) index for (a) $AE < 100$ nT, (b) $100 < AE < 300$ nT and (c) $AE > 300$ nT. Figure from Douma et al. (2017).

344 ionized at < 100 km altitudes, with higher energy electrons penetrating closer to
 345 the surface. The resulting chemical reaction of microburst electrons impacting the
 346 atmosphere produces odd hydrogen HO_x and odd nitrogen NO_x molecules, which
 347 are partially responsible for destroying ozone (O_3). Seppälä et al. (2018) modeled
 348 a six hour relativistic microburst storm and found that the mesospheric ozone was
 349 reduced by 7 – 12% in the summer months and 12 – 20% in the winter months, so
 350 microbursts may have a non-negligible contribution to the dynamics of atmospheric
 351 ozone. Furthermore, microbursts have also been estimated to have a significant
 352 impact on the outer radiation belt electron population. Radiation belt electron loss
 353 due to microbursts has been estimated to be on the order of a day (Breneman
 354 et al., 2017; Douma et al., 2019; Lorentzen et al., 2001b; O'Brien et al., 2004; Thorne
 355 et al., 2005).

356 The wave-particle interactions responsible for generating microbursts are also
 357 believed to accelerate electrons in the radiation belts. As mentioned earlier, when
 358 an electron is in resonance with a wave, energy is exchanged with the wave and
 359 the electron is either accelerated or decelerated. The signature of wave-particle

360 acceleration been observed for radiation belt electrons (e.g. Horne et al., 2005;
 361 Meredith et al., 2002; Reeves et al., 2013), and O'Brien et al. (2003) presented evidence
 362 that enhancements in chorus waves, microbursts, and radiation belt electrons are
 363 related. To explain their observations, O'Brien et al. (2003) proposed that microburst
 364 precipitation is a side effect of electron acceleration due to chorus waves.

365 The widely used theoretical framework to model the wave-particle interactions
 366 responsible for accelerating electrons and scattering microbursts is quasi-linear
 367 diffusion (e.g. Horne et al., 2005; Meredith et al., 2002; Summers, 2005; Summers
 368 et al., 1998; Thorne et al., 2005; Walker, 1993). This framework is explained in
 369 Chapter ??, and applied to an observation of a microburst in the heart of the
 370 radiation belt. Qualitatively, when a particle is resonant with a wave it can either
 371 be transported in pitch angle towards the loss cone and lose energy to the wave, or
 372 transported away from the loss cone and gain energy from the wave.

373 As previously mentioned, the range of observed microburst energies range from a
 374 few tens of keV (e.g Datta et al., 1997; Parks, 1967) to greater than 1 MeV (e.g. Blake
 375 et al., 1996; Greeley et al., 2019). The microburst electron flux (J) falls off in energy,
 376 and the microburst energy spectra is typically well fit to a decaying exponential

$$J(E) = J_0 e^{-E/E_0} \quad (1.23)$$

377 where J_0 is the flux at 0 keV (unphysical free parameter) and E_0 quantifies the
 378 efficiency of the scattering mechanism in energy (e.g. Datta et al., 1997; Lee et al.,
 379 2005; Parks, 1967). A small E_0 suggests that mostly low energy particles are scattered.
 380 In contrast a high E_0 suggests that the scattering mechanism scatters low and high
 381 energy electrons. Reality is a bit more messy and a high E_0 may be a signature of
 382 a scattering mechanism preferential to high energy electrons, but is hidden by the

convolution of the source particles available to be scattered (typically with a falling energy spectrum) and the energy-dependent efficiency of the scattering mechanism.

The short microburst duration observed by a single LEO satellite has an ambiguity when interpreting what is exactly a microburst. The two possible realities are: a microburst is very small and spatially stationary so that the LEO spacecraft passes through it in less than a second. Alternatively, microbursts are spatially large and transient so a microburst will pass by the spacecraft in a fraction of a second. There are a few ways to distinguish between the two possible realities, and each one has a unique set of advantages.

A high altitude balloon provides essentially a stationary view of the precipitating particles under the radiation belt footprints. A short-lived, temporal microburst can be unambiguously identified. Spatial structures, on the other hand, are difficult to identify because a balloon is essentially still on drift timescales.

396 Multi-spacecraft missions are an alternate solution that can determine if a
397 microburst is spatial or temporal. As will be shown in this dissertation, if a microburst
398 is observed simultaneously by two spacecraft then it is temporal and has a size
399 greater than the spacecraft separation. On the contrary, if two spacecraft observe
400 a microburst-like feature at different times but at the same location, then the feature
401 is spatial and may be a curtain (Blake and O'Brien, 2016). Both balloon and multi-
402 spacecraft observational methods have a unique set of strengths, and this dissertation
403 takes the multi-spacecraft approach to identify and study microbursts.

Scope of Research

This dissertation furthers our understanding of the microburst scattering mechanism by presenting observational evidence of microburst scattering directly, and measuring microburst sizes and comparing them to the size of chorus waves. Chapter

408 ?? describes a microburst scattering event observed by NASA’s Van Allen Probes.
409 For this event, particle and wave measurements were analyzed and modeled in the
410 theoretical framework of pitch angle and energy diffusion. Then the following two
411 chapters present studies of microburst sizes in comparison to chorus waves. Chapter
412 ?? describes a bouncing packet microburst observation made by the FIREBIRD-II
413 mission where the microburst’s lower bound longitudinal and latitudinal sizes were
414 estimated. Then Chapter ?? expands the case study from Chapter ?? to a statistical
415 study of microburst sizes using The Aerospace Corporation’s AeroCube-6 (AC6)
416 CubeSats. In this study, a Monte Carlo and analytic microburst size models were
417 developed to account for the compounding statistical effects of random microburst
418 sizes and locations. Lastly, Chapter ?? will summarize this work and make concluding
419 remarks regarding outstanding questions in microburst physics.

Bibliography

- 421 Anderson, B., Shekhar, S., Millan, R., Crew, A., Spence, H., Klumpar, D., Blake, J.,
 422 O'Brien, T., and Turner, D. (2017). Spatial scale and duration of one microburst
 423 region on 13 August 2015. *Journal of Geophysical Research: Space Physics*.
- 424 Anderson, K. A. and Milton, D. W. (1964). Balloon observations of X rays in the
 425 auroral zone: 3. High time resolution studies. *Journal of Geophysical Research*,
 426 69(21):4457–4479.
- 427 Barcus, J., Brown, R., and Rosenberg, T. (1966). Spatial and temporal character of
 428 fast variations in auroral-zone x rays. *Journal of Geophysical Research*, 71(1):125–
 429 141.
- 430 Baumjohann, W. and Treumann, R. A. (1997). *Basic space plasma physics*. World
 431 Scientific.
- 432 Blake, J.,Looper, M., Baker, D., Nakamura, R., Klecker, B., and Hovestadt, D.
 433 (1996). New high temporal and spatial resolution measurements by sampex of the
 434 precipitation of relativistic electrons. *Advances in Space Research*, 18(8):171 – 186.
- 435 Blake, J. B. and O'Brien, T. P. (2016). Observations of small-scale latitudinal
 436 structure in energetic electron precipitation. *Journal of Geophysical Research: Space
 437 Physics*, 121(4):3031–3035. 2015JA021815.
- 438 Blum, L., Li, X., and Denton, M. (2015). Rapid MeV electron precipitation as
 439 observed by SAMPEX/HILT during high-speed stream-driven storms. *Journal of
 440 Geophysical Research: Space Physics*, 120(5):3783–3794. 2014JA020633.
- 441 Breneman, A., Crew, A., Sample, J., Klumpar, D., Johnson, A., Agapitov, O.,
 442 Shumko, M., Turner, D., Santolik, O., Wygant, J., et al. (2017). Observations
 443 directly linking relativistic electron microbursts to whistler mode chorus: Van allen
 444 probes and FIREBIRD II. *Geophysical Research Letters*.
- 445 Breneman, A. W., Halford, A., Millan, R., McCarthy, M., Fennell, J., Sample, J.,
 446 Woodger, L., Hospodarsky, G., Wygant, J. R., Cattell, C. A., et al. (2015). Global-
 447 scale coherence modulation of radiation-belt electron loss from plasmaspheric hiss.
 448 *Nature*, 523(7559):193.
- 449 Brown, R., Barcus, J., and Parsons, N. (1965). Balloon observations of auroral zone
 450 x rays in conjugate regions. 2. microbursts and pulsations. *Journal of Geophysical
 451 Research (U.S.)*.
- 452 Capannolo, L., Li, W., Ma, Q., Shen, X.-C., Zhang, X.-J., Redmon, R., Rodriguez,
 453 J., Engebretson, M., Kletzing, C., Kurth, W., et al. (2019). Energetic electron
 454 precipitation: multi-event analysis of its spatial extent during emic wave activity.
 455 *Journal of Geophysical Research: Space Physics*.

- 456 Claudepierre, S., O'Brien, T.,Looper, M., Blake, J., Fennell, J., Roeder, J.,
 457 Clemmons, J., Mazur, J., Turner, D., Reeves, G., et al. (2019). A revised look
 458 at relativistic electrons in the earth's inner radiation zone and slot region. *Journal*
 459 *of Geophysical Research: Space Physics*, 124(2):934–951.
- 460 Crew, A. B., Spence, H. E., Blake, J. B., Klumpar, D. M., Larsen, B. A., O'Brien,
 461 T. P., Driscoll, S., Handley, M., Legere, J., Longworth, S., Mashburn, K.,
 462 Mosleh, E., Ryhajlo, N., Smith, S., Springer, L., and Widholm, M. (2016). First
 463 multipoint in situ observations of electron microbursts: Initial results from the
 464 NSF FIREBIRD II mission. *Journal of Geophysical Research: Space Physics*,
 465 121(6):5272–5283. 2016JA022485.
- 466 Datta, S., Skoug, R., McCarthy, M., and Parks, G. (1997). Modeling of microburst
 467 electron precipitation using pitch angle diffusion theory. *Journal of Geophysical*
 468 *Research: Space Physics*, 102(A8):17325–17333.
- 469 Douma, E., Rodger, C., Blum, L., O'Brien, T., Clilverd, M., and Blake, J. (2019).
 470 Characteristics of relativistic microburst intensity from sampex observations.
 471 *Journal of Geophysical Research: Space Physics*.
- 472 Douma, E., Rodger, C. J., Blum, L. W., and Clilverd, M. A. (2017). Occurrence
 473 characteristics of relativistic electron microbursts from SAMPEX observations.
 474 *Journal of Geophysical Research: Space Physics*, 122(8):8096–8107. 2017JA024067.
- 475 Eastwood, J., Hietala, H., Toth, G., Phan, T., and Fujimoto, M. (2015). What
 476 controls the structure and dynamics of earths magnetosphere? *Space Science*
 477 *Reviews*, 188(1-4):251–286.
- 478 Greeley, A., Kanekal, S., Baker, D., Klecker, B., and Schiller, Q. (2019). Quantifying
 479 the contribution of microbursts to global electron loss in the radiation belts. *Journal*
 480 *of Geophysical Research: Space Physics*.
- 481 Hendry, A. T., Rodger, C. J., and Clilverd, M. A. (2017). Evidence of sub-mev
 482 emic-driven electron precipitation. *Geophysical Research Letters*, 44(3):1210–1218.
- 483 Horne, R., Glauert, S., Meredith, N., Boscher, D., Maget, V., Heynderickx, D., and
 484 Pitchford, D. (2013). Space weather impacts on satellites and forecasting the earth's
 485 electron radiation belts with spacecast. *Space Weather*, 11(4):169–186.
- 486 Horne, R. B., Thorne, R. M., Shprits, Y. Y., Meredith, N. P., Glauert, S. A., Smith,
 487 A. J., Kanekal, S. G., Baker, D. N., Engebretson, M. J., Posch, J. L., et al.
 488 (2005). Wave acceleration of electrons in the van allen radiation belts. *Nature*,
 489 437(7056):227.
- 490 Kasahara, S., Miyoshi, Y., Yokota, S., Mitani, T., Kasahara, Y., Matsuda, S.,
 491 Kumamoto, A., Matsuoka, A., Kazama, Y., Frey, H., et al. (2018). Pulsating
 492 aurora from electron scattering by chorus waves. *Nature*, 554(7692):337.

- 493 Klumper, D., Springer, L., Mosleh, E., Mashburn, K., Berardinelli, S., Gunderson,
 494 A., Handly, M., Ryhajlo, N., Spence, H., Smith, S., Legere, J., Widholm, M.,
 495 Longworth, S., Crew, A., Larsen, B., Blake, J., and Walmsley, N. (2015). Flight
 496 system technologies enabling the twin-cubesat firebird-ii scientific mission.
- 497 Lee, J. J., Parks, G. K., Lee, E., Tsurutani, B. T., Hwang, J., Cho, K. S., Kim, K.-H.,
 498 Park, Y. D., Min, K. W., and McCarthy, M. P. (2012). Anisotropic pitch angle
 499 distribution of 100 keV microburst electrons in the loss cone: measurements from
 500 STSAT-1. *Annales Geophysicae*, 30(11):1567–1573.
- 501 Lee, J.-J., Parks, G. K., Min, K. W., Kim, H. J., Park, J., Hwang, J., McCarthy,
 502 M. P., Lee, E., Ryu, K. S., Lim, J. T., Sim, E. S., Lee, H. W., Kang, K. I., and
 503 Park, H. Y. (2005). Energy spectra of 170–360 keV electron microbursts measured
 504 by the korean STSAT-1. *Geophysical Research Letters*, 32(13). L13106.
- 505 Li, X., Selesnick, R., Schiller, Q., Zhang, K., Zhao, H., Baker, D. N., and Temerin,
 506 M. A. (2017). Measurement of electrons from albedo neutron decay and neutron
 507 density in near-earth space. *Nature*, 552(7685):382.
- 508 Lorentzen, K. R., Blake, J. B., Inan, U. S., and Bortnik, J. (2001a). Observations
 509 of relativistic electron microbursts in association with VLF chorus. *Journal of
 510 Geophysical Research: Space Physics*, 106(A4):6017–6027.
- 511 Lorentzen, K. R., Looper, M. D., and Blake, J. B. (2001b). Relativistic electron
 512 microbursts during the GEM storms. *Geophysical Research Letters*, 28(13):2573–
 513 2576.
- 514 Lyons, L. R. and Thorne, R. M. (1973). Equilibrium structure of radiation belt
 515 electrons. *Journal of Geophysical Research*, 78(13):2142–2149.
- 516 Meredith, N., Horne, R., Summers, D., Thorne, R., Iles, R., Heynderickx, D., and
 517 Anderson, R. (2002). Evidence for acceleration of outer zone electrons to relativistic
 518 energies by whistler mode chorus. In *Annales Geophysicae*, volume 20, pages 967–
 519 979.
- 520 Millan, R. and Thorne, R. (2007). Review of radiation belt relativistic electron losses.
 521 *Journal of Atmospheric and Solar-Terrestrial Physics*, 69(3):362 – 377.
- 522 Nakamura, R., Baker, D. N., Blake, J. B., Kanekal, S., Klecker, B., and Hovestadt,
 523 D. (1995). Relativistic electron precipitation enhancements near the outer edge of
 524 the radiation belt. *Geophysical Research Letters*, 22(9):1129–1132.
- 525 Nakamura, R., Isowa, M., Kamide, Y., Baker, D., Blake, J., and Looper, M. (2000).
 526 Observations of relativistic electron microbursts in association with VLF chorus.
 527 *J. Geophys. Res.*, 105:15875–15885.

- 528 O'Brien, T., Claudepierre, S., Blake, J., Fennell, J. F., Clemons, J., Roeder, J.,
 529 Spence, H. E., Reeves, G., and Baker, D. (2014). An empirically observed pitch-
 530 angle diffusion eigenmode in the earth's electron belt near $l^*= 5.0$. *Geophysical*
 531 *Research Letters*, 41(2):251–258.
- 532 O'Brien, T., Claudepierre, S., Guild, T., Fennell, J., Turner, D., Blake, J., Clemons,
 533 J., and Roeder, J. (2016). Inner zone and slot electron radial diffusion revisited.
 534 *Geophysical Research Letters*, 43(14):7301–7310.
- 535 O'Brien, T. and Moldwin, M. (2003). Empirical plasmapause models from magnetic
 536 indices. *Geophysical Research Letters*, 30(4).
- 537 O'Brien, T. P.,Looper, M. D., and Blake, J. B. (2004). Quantification of relativistic
 538 electron microburst losses during the GEM storms. *Geophysical Research Letters*,
 539 31(4). L04802.
- 540 O'Brien, T. P., Lorentzen, K. R., Mann, I. R., Meredith, N. P., Blake, J. B., Fennell,
 541 J. F., Looper, M. D., Milling, D. K., and Anderson, R. R. (2003). Energization of
 542 relativistic electrons in the presence of ULF power and MeV microbursts: Evidence
 543 for dual ULF and VLF acceleration. *Journal of Geophysical Research: Space*
 544 *Physics*, 108(A8).
- 545 Ozaki, M., Miyoshi, Y., Shiokawa, K., Hosokawa, K., Oyama, S.-i., Kataoka, R.,
 546 Ebihara, Y., Ogawa, Y., Kasahara, Y., Yagitani, S., et al. (2019). Visualization of
 547 rapid electron precipitation via chorus element wave–particle interactions. *Nature*
 548 *communications*, 10(1):257.
- 549 Parks, G. K. (1967). Spatial characteristics of auroral-zone X-ray microbursts. *Journal*
 550 *of Geophysical Research*, 72(1):215–226.
- 551 Reeves, G., Spence, H. E., Henderson, M., Morley, S., Friedel, R., Funsten, H., Baker,
 552 D., Kanekal, S., Blake, J., Fennell, J., et al. (2013). Electron acceleration in the
 553 heart of the van allen radiation belts. *Science*, 341(6149):991–994.
- 554 Reeves, G. D., McAdams, K. L., Friedel, R. H. W., and O'Brien, T. P. (2003). Ac-
 555 celeration and loss of relativistic electrons during geomagnetic storms. *Geophysical*
 556 *Research Letters*, 30(10):n/a–n/a. 1529.
- 557 Schulz, M. and Lanzerotti, L. J. (1974). *Particle Diffusion in the Radiation Belts*.
 558 Springer.
- 559 Seppälä, A., Douma, E., Rodger, C., Verronen, P., Clilverd, M. A., and Bortnik, J.
 560 (2018). Relativistic electron microburst events: Modeling the atmospheric impact.
 561 *Geophysical Research Letters*, 45(2):1141–1147.

- 562 Spence, H. E., Blake, J. B., Crew, A. B., Driscoll, S., Klumpar, D. M., Larsen,
 563 B. A., Legere, J., Longworth, S., Mosleh, E., O'Brien, T. P., Smith, S., Springer,
 564 L., and Widholm, M. (2012). Focusing on size and energy dependence of electron
 565 microbursts from the van allen radiation belts. *Space Weather*, 10(11).
- 566 Summers, D. (2005). Quasi-linear diffusion coefficients for field-aligned electro-
 567 magnetic waves with applications to the magnetosphere. *Journal of Geophysical
 568 Research: Space Physics*, 110(A8):n/a–n/a. A08213.
- 569 Summers, D., Thorne, R. M., and Xiao, F. (1998). Relativistic theory of wave-particle
 570 resonant diffusion with application to electron acceleration in the magnetosphere.
 571 *Journal of Geophysical Research: Space Physics*, 103(A9):20487–20500.
- 572 Thorne, R. M., O'Brien, T. P., Shprits, Y. Y., Summers, D., and Horne, R. B. (2005).
 573 Timescale for MeV electron microburst loss during geomagnetic storms. *Journal
 574 of Geophysical Research: Space Physics*, 110(A9). A09202.
- 575 Trefall, H., Bjordal, J., Ullaland, S., and Stadsnes, J. (1966). On the extension of
 576 auroral-zone x-ray microbursts. *Journal of Atmospheric and Terrestrial Physics*,
 577 28(2):225–233.
- 578 Tsurutani, B. T. and Lakhina, G. S. (1997). Some basic concepts of wave-particle
 579 interactions in collisionless plasmas. *Reviews of Geophysics*, 35(4):491–501.
- 580 Ukhorskiy, A. Y., Anderson, B. J., Brandt, P. C., and Tsyganenko, N. A. (2006).
 581 Storm time evolution of the outer radiation belt: Transport and losses. *Journal of
 582 Geophysical Research: Space Physics*, 111(A11):n/a–n/a. A11S03.
- 583 Van Allen, J. A. (1959). The geomagnetically trapped corpuscular radiation. *Journal
 584 of Geophysical Research*, 64(11):1683–1689.
- 585 Vernov, S. and Chudakov, A. (1960). Investigation of radiation in outer space. In
 586 *International Cosmic Ray Conference*, volume 3, page 19.
- 587 Walker, A. D. M. (1993). *Plasma waves in the magnetosphere*, volume 24. Springer
 588 Science & Business Media.